의학석사 학위논문

FN13762 쥐 유방암 모델에서 복셀 내 화소 결집 운동 확산 강조 자기 공명 영상에서의 정량적 히스토그램 및 텍스처 파라미터의 재현성 평가

Reproducibility of Quantitative Histogram and Texture parameters from Intravoxel Incoherent Motion Diffusion-weighted MR Imaging in FN13762 Rat Breast Cancer Model

2014년 2월

서울대학교 대학원

의학과 영상의학 전공

송 용 섭

의학석사 학위논문

FN13762 쥐 유방암 모델에서 복셀 내 화소 결집 운동 확산 강조 자기 공명 영상에서의 정량적 히스토그램 및 텍스처 파라미터의 재현성 평가

Reproducibility of Quantitative Histogram and Texture parameters from Intravoxel Incoherent Motion Diffusion-weighted MR Imaging in FN13762 Rat Breast Cancer Model

2014년 2월

서울대학교 대학원

의학과 영상의학 전공

송 용 섭

A thesis of the Master's degree

Reproducibility of Quantitative Histogram and Texture parameters from Intravoxel Incoherent Motion Diffusion-weighted MR Imaging in FN13762 Rat Breast Cancer Model

FN13762 쥐 유방암 모델에서 복셀 내 화소 결집 운동 확산 강조 자기 공명 영상에서의 정량적 히스토그램 및 텍스처 파라미터의 재현성 평가

February 2014

The Department of Radiology
Seoul National University
College of Medicine
Yong Sub Song

FN13762 쥐 유방암 모델에서 복셀 내 화소 결집 운동 확산 강조 자기 공명 영상에서의 정량적 히스토그램 및 텍스처 파라미터의 재현성 평가

지도교수 구 진 모

이 논문을 의학석사 학위논문으로 제출함

2013년 10월

서울대학교 대학원

의학과 영상의학과 전공

송 용 섭

송용섭의 의학석사 학위논문을 인준함

2014년 1월

위 원 장 김 현 진 (인)

부위원장 구 진 모 (인)

위 원 박 창 민 (인)

Reproducibility of Quantitative Histogram and Texture parameters from Intravoxel Incoherent Motion Diffusion-weighted MR Imaging in FN13762 Rat Breast Cancer Model

by

Yong Sub Song

A Thesis Submitted to the Department of Medical Science in Partial Fulfilment of the Requirements for the Degree of Master of Science in Medical Science (Major in Radiology) at the Seoul National University College of Medicine

January 2014

Approved by thesis committee:

Professor _____ Chairman

Professor _____ Vice Chair man

Professor _____

ABSTRACT

Purpose: To determine the reproducibility of quantitative histogram and texture parameters from intravoxel incoherent motion (IVIM) diffusion-weighted magnetic resonance (MR) imaging in a FN13762 breast cancer in rats.

Materials and Methods: This study was approved by the institutional animal care and use committee. FN13762 murine mammary carcinoma cell (5×10^6) were inoculated into the right upper thigh of Fisher 344 rats (n=11). At nine days after tumor implantation, IVIM diffusion-weighted MR imaging was performed twice with nine b values by using a 3-T MR imaging system. The entire tumors were manually segmented and their computerized histogram and texture parameters were automatically extracted from the apparent diffusion coefficient (ADC) and IVIM-derived parametric maps including true diffusion coefficient (D_t), pseudo-diffusion coefficient (D_p) and perfusion fraction (Pf) map using in-house software program. Intraobserver and interscan measurement reproducibility were evaluated using paired *t*-test, intraclass correlation coefficient (ICC) and Bland-Altman method. Any parameter that satisfied the lower limit of the 95% confidence interval (CI) for ICC $\geq$0.75 and absence of a systemic bias on both intraobserver and interscan comparison was designated as a reproducible parameter.

Results: Volume measurements showed good intraobserver and interscan

agreement (lower limit of the 95% CI for ICC, 0.97 and 0.95, respectively) without any systemic bias. The mean value, entropy, 5th, 10th, 25th and 90th percentile values from ADC map and the mean value, entropy, gray-level co-occurrence matrix (GLCM) contrast, 5th, 10th, 25th and 50th percentile values from D_t map showed good intraobserver and interscan agreement (lower limit of the 95% CI for ICC, $\geq$0.75) without any systemic bias. All parameters from D_p and *Pf* map showed relatively poor intraobserver and interscan agreement (lower limit of the 95% CI for ICC, <0.75).

Conclusion: In conclusion, histogram and texture analysis on ADC and D_t map were more favorable than D_p and *Pf* map in terms of measurement reproducibility. Among histogram and texture parameters, the mean, entropy, 5th, 10th, 25th and 90th percentile value from ADC map and the mean, entropy, GLCM contrast, 5th, 10th, 25th and 50th percentile value from D_t map were reproducible.

……

Keywords: reproducibility, histogram, texture, intravoxel incoherent motion, diffusion-weighted imaging, FN13762 rat breast cancer

***Student Number*:** 2012-21696

CONTENTS

LIST OF TABLES

LIST OF FIGURES

INTRODUCTION

Quantitative analysis of the apparent diffusion coefficient (ADC) map provided by diffusion-weighted magnetic resonance (MR) imaging have been a promising tool in oncologic field for differentiating malignant from benign tumor, monitoring treatment response, detecting residual tumor or recurrence and predicting treatment outcome (1-7). ADC measurement can provide valuable additional information to conventional anatomic imaging because ADC reflects the mobility of water molecules within tissue and thus can sensitively detect the increased cellularity, restriction of cellular membrane permeability and disruption of cellular membrane depolarization, all of which are common pathological changes seen in malignancies (8-11).

With advances in knowledge for diffusion-weighted MR imaging, is has been reported that the calculated ADC value is sensitive to capillary perfusion, which represents bulk motion of intravascular water protons within imaging voxels (12-15). In 1986, Le Bihan et al (12) defined intravoxel incoherent motion (IVIM) as the microscopic translational motions that occur in each image voxel in MR imaging. These motions include molecular diffusion of water and microcirculation of blood in the capillary vessels. The microcirculation caused by the blood in capillaries can also be considered as an incoherent motion because the network of capillaries within the voxel size is randomly distributed. Both “diffusion”, caused by thermal Brownian motion, and “perfusion”, caused by the microcirculation in capillaries, account for the biexponential decay of the signal observed on diffusion-weighted imaging when multiple b values are applied (12-16). Because perfusion

of blood within capillaries has no specific orientation, the perfusion can be regarded as a type of "pseudo-diffusion", which depends on the velocity of the flowing blood and the vascular architecture. The signal attenuation caused by the effect of the pseudo-diffusion depends on b value. However, the rate of signal attenuation resulting from pseudo-diffusion is usually greater than tissue diffusion because of greater distances of proton displacement during the application of the motion-probing gradients (17). Thus, in normal perfused tissue at higher b values, pseudo-diffusion accounts for only a small proportion of the measured signal in each imaging voxel. However, at lower b values, blood magnetization dominates the signal attenuation; therefore, its relative contribution to the diffusion-weighted MR signal becomes significant (17, 18). The IVIM technique applies a biexponential function to describe the measured signal attenuation at diffusion-weighted MR imaging as a mixture of tissue perfusion and tissue diffusivity effects. Consequentially, the IVIM diffusion-weighted MR imaging can calculate quantitative parameters that represent tissue water diffusivity, tissue perfusion (pseudo-diffusion coefficient) and perfusion fraction of tissues, which can also be displayed as parametric maps (17). Several authors showed clinical potential of quantitative analysis of parametric maps derived by IVIM diffusion-weighted MR imaging in evaluating liver cirrhosis, hepatic focal lesion, focal pancreatic lesion and salivary gland tumor (19-22).

Conventional quantitative analysis of ADC map and parametric maps derived by IVIM diffusion-weighted MR imaging was limited to the measurement of the mean pixel value within a region of interest (ROI) on the map. Recently, however, more sophisticated analyses such as histogram and texture analysis have been applied to the ADC map and the parametric maps derived IVIM diffusion-weighted MR

imaging and shown comparable or superior performances as imaging biomarkers for evaluating fibrosis stage and inflammatory activity of chronic hepatitis, differentiating grade of glioma, monitoring treatment response in patients with glioblastoma (23-26). Further studies validating variable histogram or texture parameters may discover additional imaging biomarkers which can provide additional information through noninvasive assessment of a target lesion. Those attempts may be successfully achieved by meticulously performing an animal experiment with prospective design because pathological background of an eligible imaging biomarker can be more easily evaluated than human study (27, 28). However, reproducibility test of an eligible imaging biomarker should precede an animal experiment as well as a clinical trial because accurate measures of precision error are essential for knowing the magnitude of change in values of the eligible imaging biomarker that can be detected confidently (29).

To our knowledge, there have been few studies on reproducibility test of histogram and texture parameters from ADC map (23, 30) and there have been no studies on reproducibility test of those parameters from any parametric maps derived by IVIM MR imaging. Thus, the purpose of our study was to determine the reproducibility of quantitative histogram and texture parameters from IVIM diffusion-weighted MR imaging in a FN13762 breast cancer in rats.

MATERIALS AND METHODS

This study was approved by the Animal Care and Use Committee of Seoul National University Hospital.

Tumor cell cline, Experimental animals and Tumor implantation

We used the FN13762 murine mammary carcinoma cell line (31) (American Type Culture Collection, Manassas, Va) as an experimental animal tumor model. The FN13762 carcinoma, a spontaneously metastatic syngeneic rat tumor, has been extensively characterized for both its in vitro and in vivo growth (32). The line was established in female Fischer 344 rats by administration of 7, 12-dimethylbenz(a)anthracene (32).

Eleven female Fischer 344 rats (weight range, 250-300g; Charles River, Sulzbach, Germany) were used for our study. For tumor cell implantation, the subjects were anesthetized by injecting a solution of zolazepam (5 mg/kg, Zoletil® ; Virbac, Carros, France) and xylazine (10 mg/kg, Rompun® ; Bayer-Schering Pharma, Berlin, Germany) into the hindlimb. After anesthesia, FN13762 cells were inoculated into the muscular layer of the right upper thigh of the rats with a 24-guage needle by injecting 5×10^6 cells suspended in 0.1 mL Dulbecco's modified Eagle's medium (Cambrex Biosciences, Verviers, France). Cellular viability was tested prior to tumor implantation by using trypan blue; this always yielded a result greater than 90%. All procedures were performed by using aseptic technique. Animals were monitored through the recovery period and were returned to their cages.

MR Imaging Acquisition

After the 9-day feeding period, MR imaging scans were performed with a 3-T MR imaging system (TrioTim; Siemens Medical Solutions, Erlangen, Germany) with a 6-channel rat body coil (Stark Contrast, Erlangen, Germany). The animals were anesthetized by injecting a solution of zolazepam (5 mg/kg, Zoletil® ; Virbac, Carros, France) and xylazine (10 mg/kg, Rompun® ; Bayer-Schering Pharma, Berlin, Germany) into the hindlimb. At first, we acquired axial T2-weighted turbo spin echo images (TR/TE, 8930/101 ms; bandwidth, 196 Hz/pixel; flip angle, 120°; field of view, 100×81 mm; matrix, 192×115; slice thickness, 0.8 mm; number of signals acquired, eight) of lower-half body of the rat. For IVIM diffusion-weighted MR imaging, a radiology resident (Y.S.S.) reviewed T2-weighted images and determined scan range to cover the entire volume of the tumor. IVIM diffusion-weighted MR images were acquired by using a free-breathing single-shot echo-planar imaging pulse sequence with diffusion gradients applied in three orthogonal directions with the following parameters: TR/TE, 4400 /73 ms; bandwidth, 798 Hz/pixel; field of view, 100×100 mm; matrix, 128×128; section thickness, 3 mm; number of signals acquired, eight; and multiple b values, 0, 25, 50, 75, 100, 200, 400, 800 and 1000 sec/mm^2. To shorten the echo train length, the parallel imaging technique (generalized autocalibrating partially parallel acquisitions; GRAPPA) with a 2-fold acceleration factor was used. To assess the interscan reproducibility of parameters from the IVIM diffusion-weighted MR imaging, all rats underwent IVIM diffusion-weighted MR imaging twice, with the examinations 5 minutes apart.

IVIM Parametric Map Acquisition

Diffusion-weighted MR imaging data were post-processed by using prototype software (Siemens Healthcare, Erlangen, Germany) to extract the ADC and IVIM parameters composed of the true diffusion coefficient (D_t), representing pure molecular diffusibility; pseudo-diffusion coefficient (D_p), representing perfusion-related incoherent microcirculation; and perfusion fraction (Pf), which is linked to blood volume (33). ADC values were automatically calculated by using all b values with a monoexponential fit with the following equation: $SI/SI_0 = \exp(-b \cdot ADC)$, where SI_0 is the mean signal intensity of the ROI for a b value of 0 sec/mm^2 and SI is the signal intensity for the higher b value. On the basis of the IVIM concept, the D_t, D_p and Pf values were calculated by using a nonlinear biexponential fit according to the following equation (29): $SI/SI_0 = (1 - Pf) \cdot \exp(-b \cdot D_t) + Pf \cdot \exp(-b \cdot D_p)$. Four parametric maps of ADC, D_t, D_p and Pf were created on a pixel-by-pixel basis for each animal (Fig 1).

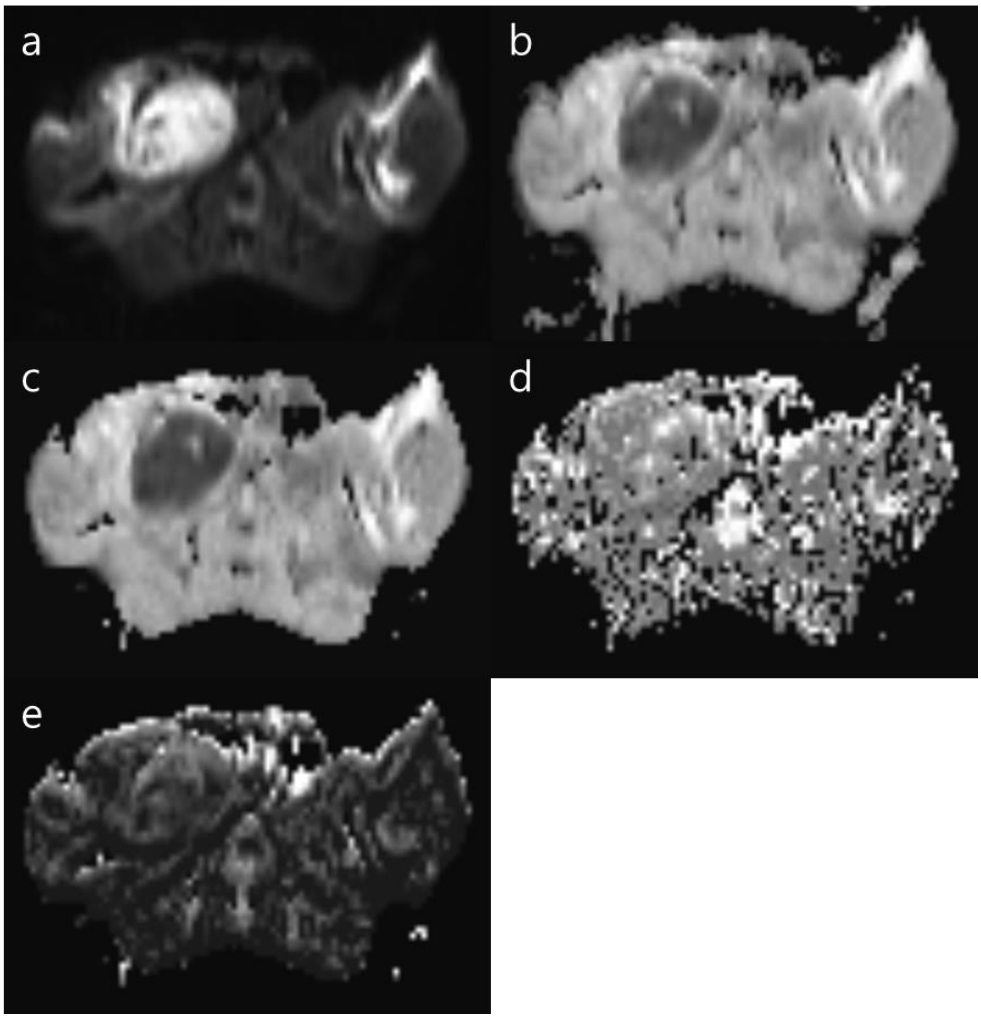

Figure 1. FN13762 breast cancer in a rat model. (a) Axial diffusion-weighted image of the tumor in the right hindlimb (b = 200 sec/mm^2) and (b) corresponding ADC map. IVIM diffusion-weighted imaging parametric maps of (c) D_t, (d) D_p and (e) *Pf*.

Image Analysis

One radiology resident (Y.S.S with 3 years of experience in body MR imaging) manually drew ROI to encompass as much of the whole tumor as possible on all the ADC maps from the first IVIM MR imaging by using in-house software (Fig 2).

Care was taken to avoid non-tumor tissues on the ADC maps. To evaluate the intraobserver and interscan reproducibility of parameters from the IVIM diffusion-weighted MR imaging, the same observer drew ROIs of whole tumors on the ADC maps from the first and the second IVIM MR imaging, at each one-week interval. The ROIs were then copied from the ADC map and placed on the other corresponding parametric maps for D_t, D_p and Pf. After a ROI was placed, ROI volume, histogram and texture parameters were calculated and extracted automatically. Histogram parameters included: (a) mean, (b) standard deviation (SD), (c) skewness, (d) kurtosis and (e) percentile values (5th, 10th, 25th, 50th, 75th and 90th). Texture parameters included: (a) entropy, (b) homogeneity, (c) gray-level co-occurrence matrix (GLCM) inverse difference moment (IDM) and (d) and GLCM contrast. Detail methods for calculating skewness, kurtosis, entropy, homogeneity, GLCM IDM and GLCM contrast from images were described in APPENDIX.

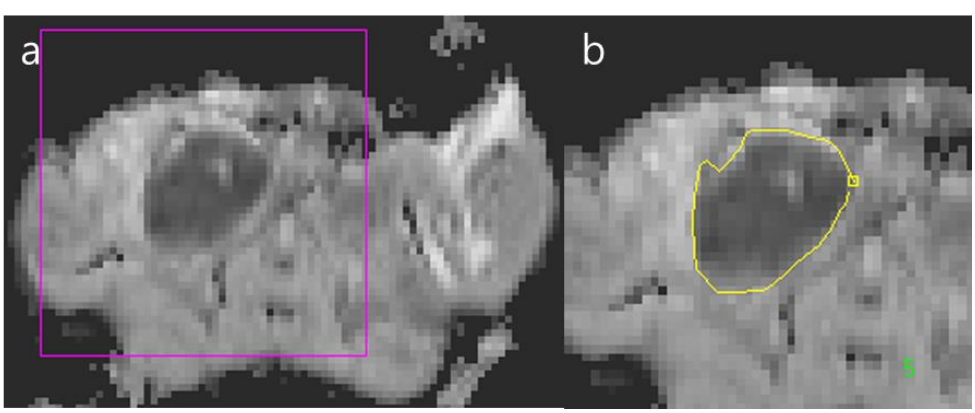

Figure 2. In-house software program for histogram and texture parameter measurement. This software program provides two screens of loaded MR images with or without magnification. (a) Larger screen shows a loaded ADC map without magnification. The area within the purple square is selected for magnification. (b)

Smaller screen shows a 1.3-fold magnified image of the area within the purple square selected on the larger screen. Region-of-interest (shown as polymorphic yellow line; the small yellow square on the yellow line means the starting point of region-of-interest drawing) was performed on this magnified image. The green number on the image means the current image number of the ADC map stack.

Statistical analysis

We compared all parameters between the first measurement and the second measurement on the first IVIM MR imaging for the intraobserver reproducibility test, and between the first measurement on the first IVIM MR imaging and the second IVIM MR imaging for the interscan reproducibility test.

A paired *t* test was used to assess the presence of any systemic bias in intraobserver and interscan comparison for all parameters. The results with *P*-values of <0.05 were considered statistically significant. The reproducibilities of all parameters were then evaluated by using the intraclass correlation coefficient (ICC). The lower limit of the 95% confidence interval (CI) for ICC ≥ 0.75 was considered to represent good agreement (34). We designated each parameter as a reproducible parameter when all following conditions were satisfied in both intraobserver and interscan comparison: (a) no systemic bias according to the paired *t* test and (b) good agreement according to the ICC. To estimate the magnitude of measurement variability in all parameters, the 95% limits of agreement in intraobserver and interscan comparison were obtained according to the Bland-Altman method (35). The results of the Bland-Altman method were expressed as absolute values for skewness, kurtosis, entropy, homogeneity, GLCM IDM and GLCM contrast and

transformed as percentages for mean, SD and percentile values because variabilities of those parameters were not independent of the magnitude of the measurement.

All statistical analyses were performed using Medcalc (version 12.7.2.0, MedCalc Software, Mariakerke, Belgium).

Results

The mean diameter of all 11 tumors was 14.36 mm ± 3.00 mm (range, 10.63-19.72 mm). As for volume measurements, there were no significant mean differences in terms of intraobserver variability nor interscan variability and their ICCs were 0.99 (95% CI, 0.97-1.00) and 0.99 (95% CI, 0.95-1.00) for intraobserver and interscan comparison, respectively. The 95% limits of agreement in intraobserver and interscan comparison ranged from -18.2% to 18.0% (mean, -0.1%) and -27.5% to 25.7% (mean, -0.9%) of the ROI volumes, respectively.

ADC map

There was no significant difference in mean of all parameters from the ADC maps in terms of both intraobserver and interscan comparison. Table 1 summarizes the results of ICCs and Bland-Altman methods in intraobserver and interscan comparison for all parameters from the ADC maps. For intraobserver comparison, mean, entropy, GLCM contrast and all percentile values showed good agreement, with lower limits of 95% CI for ICC ranging from 0.85 to 1.00. For interscan comparison, mean, entropy, 5th, 10th, 25th and 90th percentile value showed good agreement, with lower limits of 95% CI for ICC ranging from 0.77 to 0.94.

Table 1. Results of intraclass correlation coefficient and Bland-Altman method for all parameters from ADC map

	Intraobserver reproducibility test				Interscan reproducibility test			
			Bland-Altman method				Bland-Altman method	
	ICC	95% CI	95% LOA	mean	ICC	95% CI	95% LOA	mean
Mean	0.98	0.92, 0.99	-8.28%, 8.13%	-0.08%	0.93	0.77, 0.98	-12.15%, 11.50%	-0.33%
SD	0.92	0.72, 0.98	-22.33%, 24.30%	0.98%	0.91	0.72, 0.98	-20.59%, 20.82%	0.11%
Skewness†	0.89	0.64, 0.97	-0.304, 0.406	0.051	0.86	0.56, 0.96	-0.255, 0.504	0.125
Kurtosis†	0.91	0.69, 0.97	-0.882, 1.187	0.153	0.91	0.72, 0.98	-0.630, 1.227	0.299
Entropy†	0.98	0.91, 0.99	-0.175, 0.187	0.006	0.96	0.86, 0.99	-0.249, 0.213	-0.018
Homogeneity†	0.90	0.66, 0.97	-0.004, 0.005	0.000	-0.12	-0.65, 0.49	-0.019, 0.017	-0.001
GLCM IDM†	0.92	0.72, 0.98	-0.004, 0.003	0.000	-0.20	-0.69, 0.43	-0.017, 0.014	-0.002
GLCM Contrast†	0.98	0.92, 0.99	-2.664, 2.470	-0.097	0.92	0.72, 0.98	-6.078, 5.188	-0.445
5th percentile	1.00	0.99, 1.00	-3.29%, 3.65%	0.18%	0.97	0.90, 0.99	-6.84%, 11.59%	2.38%
10th percentile	1.00	1.00, 1.00	-1.68%, 2.51%	0.42%	0.98	0.94, 1.00	-5.68%, 9.38%	1.85%
25th percentile	0.99	0.98, 1.00	-5.30%, 5.45%	0.07%	0.97	0.90, 0.99	-10.40%, 10.38%	-0.01%
50th percentile	0.96	0.86, 0.99	-11.88%, 10.71%	-0.59%	0.92	0.74, 0.98	-16.67%, 12.78%	-1.95%
75th percentile	0.97	0.91, 0.99	-7.91%, 7.91%	0.00%	0.89	0.63, 0.97	-16.00%, 12.60%	-1.70%
90th percentile	0.96	0.85, 0.99	-12.75%, 12.51%	-0.12%	0.94	0.79, 0.98	-13.78%, 13.78%	0.00%

Note.—ICC = intraclass correlation coefficient, CI = confidence interval, LOA = limit of agreement, SD = standard deviation, GLCM = gray-level co-occurrence matrix and IDM = inverse difference moment.

† Expressed as an absolute value in Bland-Altman method.

D_t map

There was significance difference in kurtosis in terms of interscan comparison (P=0.034). Table 2 summarizes the results of ICCs and Bland-Altman methods in intraobserver and interscan comparison for all parameters from the D_t maps. For intraobserver comparison, mean, entropy, GLCM contrast and all percentile values showed good agreement, with lower limits of 95% CI for ICC ranging from 0.87 to 1.00. For interscan comparison, mean, entropy, GLCM contrast, 5th, 10th, 25th and 50th percentile value showed good agreement, with lower limits of 95% CI for ICC ranging from 0.77 to 0.96.

Table 2. Results of intraclass correlation coefficient and Bland-Altman method for all parameters from D_t map

	Intraobserver reproducibility test				Interscan reproducibility test			
			Bland-Altman method				Bland-Altman method	
	ICC	95% CI	95% LOA	mean	ICC	95% CI	95% LOA	mean
Mean	0.98	0.92, 0.99	-8.84%, 8.47%	-0.19%	0.95	0.81, 0.99	-11.51%, 10.70%	-0.40%
SD	0.91	0.70, 0.97	-24.25%, 26.46%	1.11%	0.90	0.68, 0.97	-22.99%, 21.93%	-0.53%
Skewness†	0.91	0.70, 0.97	-0.318, 0.390	0.036	0.87	0.58, 0.96	-0.290, 0.516	0.113
Kurtosis†	0.89	0.66, 0.97	-1.054, 1.424	0.185	0.92	0.73, 0.98	-0.646, 1.429	0.391
Entropy†	0.97	0.89, 0.99	-0.191, 0.187	-0.002	0.97	0.90, 0.99	-0.199, 0.169	-0.015
Homogeneity†	0.90	0.66, 0.97	-0.003, 0.002	-0.001	-0.36	-0.77, 0.27	-0.016, 0.013	-0.002
GLCM IDM†	0.83	0.48, 0.95	-0.003, 0.002	0.000	-0.48	-0.83, 0.13	-0.016, 0.011	-0.002
GLCM Contrast†	0.98	0.92, 0.99	-2.746, 2.465	-0.141	0.93	0.77, 0.98	-5.535, 4.612	-0.462
5th percentile	1.00	0.99, 1.00	-3.02%, 3.33%	0.15%	0.97	0.89, 0.99	-5.17%, 11.30%	3.06%
10th percentile	1.00	1.00, 1.00	-1.54%, 1.89%	0.18%	0.99	0.96, 1.00	-4.21%, 8.43%	2.11%
25th percentile	1.00	0.98, 1.00	-5.48%, 4.33%	-0.58%	0.98	0.92, 0.99	-8.03%, 9.60%	0.78%
50th percentile	0.96	0.87, 0.99	-12.45%, 10.60%	-0.92%	0.95	0.84, 0.99	-13.66%, 10.33%	-1.67%
75th percentile	0.98	0.93, 0.99	-8.42%, 7.19%	-0.62%	0.91	0.72, 0.98	-15.56%, 10.69%	-2.44%
90th percentile	0.97	0.88, 0.99	-11.67%, 12.05%	0.19%	0.92	0.73, 0.98	-16.57%, 15.07%	-0.75%

Note.—ICC = intraclass correlation coefficient, CI = confidence interval, LOA = limit of agreement, SD = standard deviation, GLCM = gray-level co-occurrence matrix and IDM = inverse difference moment.

† Expressed as an absolute value in Bland-Altman method.

D_p map

There was no significant difference in mean of all parameters from the D_p maps in terms of both intraobserver and interscan comparison. Table 3 summarizes the results of ICCs and Bland-Altman methods in intraobserver and interscan comparison for all parameters from the D_p maps. For intraobserver comparison, mean, kurtosis, entropy, homogeneity, GLCM IDM, 25th, 50th and 75th percentile values showed good agreement, with lower limits of 95% CI for ICC ranging from 0.77 to 0.99. For interscan comparison, however, no one parameter showed good agreement.

Table 3. Results of intraclass correlation coefficient and Bland-Altman method for all parameters from D_p map

	Intraobserver reproducibility test				Interscan reproducibility test			
			Bland-Altman method				Bland-Altman method	
	ICC	95% CI	95% LOA	mean	ICC	95% CI	95% LOA	mean
Mean	0.93	0.77, 0.98	-3.90, 5.12%	0.61%	0.59	0.03, 0.87	-15.92, 10.05%	-2.93%
SD	0.44	-0.18, 0.81	-35.58, 47.93%	6.17%	0.60	0.04, 0.87	-40.79, 29.69%	-5.55%
Skewness†	0.90	0.67, 0.97	-0.790, 0.974	0.092	0.50	-0.10, 0.84	-2.319, 1.798	-0.261
Kurtosis†	0.96	0.87, 0.99	-2.320, 1.852	-0.234	0.34	-0.29, 0.77	-9.109, 8.855	-0.127
Entropy†	0.96	0.86, 0.99	-0.163, 0.215	0.026	0.54	-0.06, 0.85	-0.650, 0.509	-0.071
Homogeneity†	0.97	0.91, 0.99	-0.005, 0.005	0.000	0.75	0.31, 0.93	-0.013, 0.017	0.002
GLCM IDM†	0.93	0.77, 0.98	-0.004, 0.003	0.000	0.32	-0.32, 0.76	-0.015, 0.015	0.000
GLCM Contrast†	0.90	0.67, 0.97	-0.331, 0.439	0.054	0.60	0.04, 0.88	-1.219, 0.768	-0.226
5th percentile	0.56	-0.03, 0.86	-308.49, 361.05%	26.28%	0.09	-0.52, 0.63	-435.73, 486.33%	25.30%
10th percentile	0.87	0.58, 0.96	-179.89, 132.81%	-23.54%	0.25	-0.39, 0.72	-496.00, 544.33%	24.17%
25th percentile	1.00	0.99, 1.00	-1.94, 2.34%	0.20%	-0.23	-0.71, 0.40	-47.98, 36.57%	-5.70%
50th percentile	0.98	0.91, 0.99	-2.36, 1.96%	-0.20%	0.56	-0.03, 0.86	-11.90, 9.55%	-1.18%
75th percentile	0.94	0.79, 0.98	-3.79, 4.85%	0.53%	0.70	0.21, 0.91	-15.29, 8.74%	-3.27%
90th percentile	0.80	0.42, 0.94	-9.13, 10.18%	0.52%	0.59	0.02, 0.87	-22.94, 12.25%	-5.34%

Note.—ICC = intraclass correlation coefficient, CI = confidence interval, LOA = limit of agreement, SD = standard deviation, GLCM = gray-level co-occurrence matrix and IDM = inverse difference moment.

† Expressed as an absolute value in Bland-Altman method.

Pf map

There was significance difference in mean in terms of intraobserver comparison (*P*=0.049). Table 4 summarizes the results of ICCs and Bland-Altman methods in intraobserver and interscan comparison for all parameters from the *Pf* maps. For intraobserver comparison, mean, 10th, 25th, 50th, 75th and 90th percentile value showed good agreement, with lower limits of 95% CI for ICC ranging from 0.87 to 1.00. For interscan comparison, however, no one parameter showed good agreement.

Table 4. Results of intraclass correlation coefficient and Bland-Altman method for all parameters from *Pf* map

	Intraobserver reproducibility test				Interscan reproducibility test			
			Bland-Altman method				Bland-Altman method	
	ICC	95% CI	95% LOA	mean	ICC	95% CI	95% LOA	mean
Mean	0.98	0.91, 0.99	-3.20%, 6.56%	1.68%	0.27	-0.36, 0.73	-34.94%, 30.29%	-2.33%
SD	0.79	0.38, 0.94	-49.63%, 75.37%	12.87%	0.50	-0.10, 0.84	-71.02%, 87.98%	8.48%
Skewness†	0.32	-0.31, 0.76	-1.110, 1.247	0.069	0.20	-0.42, 0.70	-2.107, 1.789	-0.159
Kurtosis†	0.33	-0.31, 0.76	-6.841, 6.301	-0.270	0.15	-0.47, 0.67	-20.100, 14.861	-2.620
Entropy†	-0.04	-0.60, 0.55	-1.560, 2.124	0.282	-0.06	-0.61, 0.54	-1.662, 2.177	0.258
Homogeneity†	0.52	-0.08, 0.84	-0.006, 0.009	0.002	0.37	-0.26, 0.78	-0.007, 0.011	0.002
GLCM IDM†	0.29	-0.34, 0.74	-0.001, 0.002	0.001	-0.09	-0.63, 0.51	-0.003, 0.004	0.000
GLCM Contrast†	0.02	-0.57, 0.59	-4.000, 5.528	0.764	0.01	-0.57, 0.58	-4.165, 5.533	0.684
5th percentile	0.61	0.05, 0.88	-191.46%, 192.95%	0.74%	0.07	-0.53, 0.62	-282.50%, 321.43%	19.46%
10th percentile	1.00	1.00, 1.00	-7.44%, 10.34%	1.45%	-0.09	-0.63, 0.51	-198.02%, 191.12%	-3.45%
25th percentile	0.96	0.87, 0.99	-11.17%, 10.14%	-0.52%	0.24	-0.39, 0.72	-62.85%, 48.49%	-7.18%
50th percentile	0.97	0.89, 0.99	-5.71%, 6.69%	0.49%	0.18	-0.44, 0.68	-38.63%, 31.85%	-3.39%
75th percentile	0.98	0.95, 1.00	-3.92%, 6.51%	1.29%	0.56	-0.03, 0.86	-30.42%, 25.42%	-2.50%
90th percentile	0.99	0.96, 1.00	-3.75%, 6.36%	1.30%	0.57	-0.01, 0.86	-32.29%, 31.30%	-0.49%

Note.—ICC = intraclass correlation coefficient, CI = confidence interval, LOA = limit of agreement, SD = standard deviation, GLCM = gray-level co-occurrence matrix and IDM = inverse difference moment.

† Expressed as an absolute value in Bland-Altman method.

DISCUSSION

We evaluated reproducibility of variable parameters of the ADC maps and parametric maps from IVIM diffusion-weighted MR imaging in terms of both intraobserver and interscan variability. We repeated diffusion-weighted MR imaging in a single imaging session over a very short time interval, changes in the tumor microenvironment or in the physiologic status of the animals may have been negligible, and thus, the interscan variability of the parameters in our study would reflect the measurement error that may have resulted from image noise, image distortion and motion artifacts as well as intraobserver variability for ROI drawing. Indeed, all parameters that failed to attain good intraobserver agreement also failed to attain good interscan agreement. Acceptable interscan reproducibility is an essential for an imaging biomarker because at least two sets of images scanned at different time points are needed to evaluate change in the imaging biomarker. We showed that several histogram and texture parameters can be reproducibly measured from ADC map and D_t map in FN13762 breast cancer in rats. Those parameters were the mean, entropy, 5th, 10th, 25th and 90th percentile value from ADC map, and the mean, entropy, GLCM contrast, 5th, 10th, 25th and 50th percentile value from D_t map.

The mean value have been widely used as a representative value of a target lesion in oncologic imaging (36) and good reproducibility of the mean value from ADC map and D_t map was reported in previous animal study and human study (23, 37, 38). Furthermore, the method of ROI drawing might be positively influence on reproducibility of the mean value. In this study, we calculated mean value by

averaging all pixel values from whole tumor volumes. Lambregts et al (39) reported that ADC measurements obtained from whole tumor volumes are more reproducible than those obtained from single-slice or small sample ROIs. A previous clinical trial (40) also reported good reproducibility of the ADC and perfusion-insensitive ADC value from ROIs encasing whole tumor volumes.

The entropy describes the variation in a volume histogram of pixel value and is a promising indicator for tumor heterogeneity (41). In fact, SD, homogeneity, GLCM IDM and GLCM contrast also measure a particular characteristic of the distribution between pixels in the ROI (42), thus may reflect tumor heterogeneity. Because those variables are dependent on one another, selection of fewer parameters with advantage of measurement reproducibility may be more practical approach to discover new imaging biomarkers. From our results, entropy from both ADC map and D_t map, and GLCM contrast from D_t map showed better reproducibility than other parameters. Fujimoto et al (23) showed good interobserver reproducibility of the entropy from ADC map of the liver parenchyma in patients with chronic hepatitis C and reported that the coefficient of repeatability (i.e. 1.96 times the SD of the differences between the two measurements) was 0.072. In our entropy measurement from FN13762 breast cancer in rats, the coefficients of repeatability were 0.096 and 0.118 for intraobserver and interscan comparison, respectively. Jensen et al (38) also showed good interscan reproducibility of ADC entropy of which ICC was 0.84 (CI was not presented in their paper) in breast cancer patients.

Lower percentile values (i.e. 5th, 10th and 25th percentile value) of ADC and D_t histogram have been chosen to take into account tumor heterogeneity and regarded as a promising measurement method which may sensitively defect focal regions of higher cellularity (25, 26, 43, 44). Our results showed that those parameters can be

consistently measured in both ADC and D_t histogram of a small animal tumor. Fiftieth percentile value, as well as 10th and 25th percentile value, of ADC histogram was also suggested as useful parameter in predicting low-grade glioma subtype (45), however showed relatively worse reproducibility than lower percentile values (i.e. 5th, 10th and 25th percentile value) in our study. On the other hand, fiftieth percentile value of D_t histogram showed slightly better reproducibility than that of ADC histogram. Ninetieth percentile value of ADC and D_t histogram may reflect low cellularity region within the tumor such as necrosis or cystic change (17, 36) and was slightly more reproducible in ADC histogram than D_t histogram in our study.

In our study, the kurtosis and skewness measurement from ADC histogram showed relatively worse reproducibility in FN13762 breast cancer in rat. Those parameters from ADC map were suggested as potential imaging biomarkers for predicting chemotherapy response and predicting progression free survival in various malignancies (38, 44, 46, 47). Jensen et al (38) investigated interscan reliability of ADC mean, skewness and entropy in breast cancer patients and the interscan ICC of ADC skewness (0.75; 95% CI was not presented in their paper) was relatively worse than that of ADC mean and entropy (0.84) which is compatible with our results. In addition, relatively small number of voxels within in animal tumors might enhance variability of skewness and kurtosis (48). Thus those two parameters may be more reliable in larger tumors of human patients.

All parameters in D_p map and Pf map showed relatively worse reproducibility than ADC or D_t maps. Some parameters showed good intraobserver agreement, whereas all parameters failed to attain good interscan agreement on ICC analyses. Both perfusion-sensitive parameters are calculated from biexponential fitting of

IVIM diffusion-weighted MR imaging data at multiple lower b values. However signal measurement at low b values, especially $\leq$100 sec/mm^2, are more prone to measurement errors and are highly sensitive to signal-to-noise variations, thus hindering consistent model fitting (15, 17, 49). Andreou et al (18) reported poor measurement reproducibility of mean D_p and *Pf* in liver metastases, with very wide 95% CI of the differences (-89% to +2,120% and -75.3% to +241% for D_p and *Pf*, respectively). Koh et al (40) demonstrated poor measurement reproducibility of ADC values calculated using low b values. They also showed a large SD in the estimation of *Pf* (50). In this context, they described that voxel-by-voxel analysis may be inappropriate for perfusion-sensitive parameters (17), which is supported by our results. In spite of the poor reproducibility, however, several studies reported significant differences of perfusion-sensitive parameters between variable target lesions (50-52). In colorectal liver metastases (50), the estimated *Pf* of colorectal liver metastases was significantly lower than that in normal liver parenchyma, in keeping with the hypovascular nature of these lesions. Shinmoto et al (51) reported that both fast (pseudo-diffusion) and slow (true diffusion) ADCs were lower in prostate cancer than normal peripheral or transitional zones. Lemke et al (52) demonstrated that the *Pf* of pancreatic carcinoma was significantly lower than normal pancreatic parenchyma. However, currently there is no standard vendor software for biexponential model fitting of IVIM diffusion-weighted MR imaging data and there is no consensus on the established IVIM diffusion-weighted MR imaging protocol such as number and choice of b values and number of signal averages. Indeed, previous studies (19-22, 50-52) on IVIM used variable software and imaging protocols with variable number of b values. Thus our results do not

simply implicate inferiority of perfusion-sensitive parameters from any kind of IVIM techniques and thus do not contradict previously reported usefulness of those parameters (50-52). Further study optimizing and individualizing IVIM technique may improve aforementioned measurement error of perfusion-sensitive parameters. Also, although measurement error of a certain parameter is substantial, the parameter can be used as imaging biomarker when change scale of the parameter in certain clinical situation exceeds the measurement error and vice versa. Therefore, the histogram and texture parameters from perfusion-sensitive parametric maps still have chance of clinical application despite their relatively poor reproducibility.

Our study had several limitations. First, there were a relatively small number of subjects to evaluate measurement reproducibility of the parameters from ADC map and parametric maps derived by IVIM MR imaging. Second, we performed the second IVIM MR imaging without reposition of the animals, differs from that used in actual clinical practice or animal experiment. This might overestimate interscan reproducibility of the parameters. Third, all MR scans for the tumors were performed at the same time point of the tumor growth, which might cause relatively uniform pathologic state of the tumors. This might also cause overestimation of intraobserver and interscan reproducibility of the parameters. Fourth, all parameters were measured by one observer, which can be significantly influenced by observers' subjective trend.

In conclusion, histogram and texture analysis on ADC and D_t map were more favorable than D_p and Pf map in terms of measurement reproducibility. Among histogram and texture parameters, the mean, entropy, 5th, 10th, 25th and 90th percentile value from ADC map and the mean, entropy, GLCM contrast, 5th, 10th, 25th and 50th percentile value from D_t map were reproducible.

REFERENCES

1. Sumi M, Sakihama N, Sumi T, et al. Discrimination of metastatic cervical lymph nodes with diffusion-weighted MR imaging in patients with head and neck cancer. AJNR American journal of neuroradiology. 2003;24(8):1627-34.

2. Taouli B, Vilgrain V, Dumont E, Daire JL, Fan B, Menu Y. Evaluation of liver diffusion isotropy and characterization of focal hepatic lesions with two single-shot echo-planar MR imaging sequences: prospective study in 66 patients. Radiology. 2003;226(1):71-8.

3. Thoeny HC, De Keyzer F, Chen F, et al. Diffusion-weighted MR imaging in monitoring the effect of a vascular targeting agent on rhabdomyosarcoma in rats. Radiology. 2005;234(3):756-64.

4. Thoeny HC, De Keyzer F, Chen F, et al. Diffusion-weighted magnetic resonance imaging allows noninvasive in vivo monitoring of the effects of combretastatin a-4 phosphate after repeated administration. Neoplasia. 2005;7(8):779-87.

5. Pickles MD, Gibbs P, Lowry M, Turnbull LW. Diffusion changes precede size reduction in neoadjuvant treatment of breast cancer. Magnetic resonance imaging. 2006;24(7):843-7.

6. Kamel IR, Reyes DK, Liapi E, Bluemke DA, Geschwind JF. Functional MR imaging assessment of tumor response after 90Y microsphere treatment in patients with unresectable hepatocellular carcinoma. Journal of vascular and interventional radiology : JVIR. 2007;18(1 Pt 1):49-56.

7. Yankeelov TE, Lepage M, Chakravarthy A, et al. Integration of

quantitative DCE-MRI and ADC mapping to monitor treatment response in human breast cancer: initial results. Magnetic resonance imaging. 2007;25(1):1-13.

8. Chan JH, Tsui EY, Luk SH, et al. Diffusion-weighted MR imaging of the liver: distinguishing hepatic abscess from cystic or necrotic tumor. Abdominal imaging. 2001;26(2):161-5.

9. Kamel IR, Bluemke DA, Ramsey D, et al. Role of diffusion-weighted imaging in estimating tumor necrosis after chemoembolization of hepatocellular carcinoma. AJR American journal of roentgenology. 2003;181(3):708-10.

10. Malayeri AA, El Khouli RH, Zaheer A, et al. Principles and applications of diffusion-weighted imaging in cancer detection, staging, and treatment follow-up. Radiographics : a review publication of the Radiological Society of North America, Inc. 2011;31(6):1773-91.

11. Rheinheimer S, Stieltjes B, Schneider F, et al. Investigation of renal lesions by diffusion-weighted magnetic resonance imaging applying intravoxel incoherent motion-derived parameters--initial experience. European journal of radiology. 2012;81(3):e310-6.

12. Le Bihan D, Breton E, Lallemand D, Grenier P, Cabanis E, Laval-Jeantet M. MR imaging of intravoxel incoherent motions: application to diffusion and perfusion in neurologic disorders. Radiology. 1986;161(2):401-7.

13. Le Bihan D, Breton E, Lallemand D, Aubin ML, Vignaud J, Laval-Jeantet M. Separation of diffusion and perfusion in intravoxel incoherent motion MR imaging. Radiology. 1988;168(2):497-505.

14. LeBihan D. IVIM method measures diffusion and perfusion. Diagnostic imaging. 1990;12(6):133, 6.

15. Le Bihan D, Turner R, Moonen CT, Pekar J. Imaging of diffusion and

microcirculation with gradient sensitization: design, strategy, and significance. Journal of magnetic resonance imaging : JMRI. 1991;1(1):7-28.

16. Le Bihan D. Intravoxel incoherent motion perfusion MR imaging: a wake-up call. Radiology. 2008;249(3):748-52.

17. Koh DM, Collins DJ, Orton MR. Intravoxel incoherent motion in body diffusion-weighted MRI: reality and challenges. AJR American journal of roentgenology. 2011;196(6):1351-61.

18. Andreou A, Koh DM, Collins DJ, et al. Measurement reproducibility of perfusion fraction and pseudodiffusion coefficient derived by intravoxel incoherent motion diffusion-weighted MR imaging in normal liver and metastases. Eur Radiol. 2013;23(2):428-34.

19. Yoon JH, Lee JM, Yu MH, Kiefer B, Han JK, Choi BI. Evaluation of hepatic focal lesions using diffusion-weighted MR imaging: Comparison of apparent diffusion coefficient and intravoxel incoherent motion-derived parameters. Journal of magnetic resonance imaging : JMRI. 2013.

20. Sumi M, Van Cauteren M, Sumi T, Obara M, Ichikawa Y, Nakamura T. Salivary gland tumors: use of intravoxel incoherent motion MR imaging for assessment of diffusion and perfusion for the differentiation of benign from malignant tumors. Radiology. 2012;263(3):770-7.

21. Luciani A, Vignaud A, Cavet M, et al. Liver cirrhosis: intravoxel incoherent motion MR imaging--pilot study. Radiology. 2008;249(3):891-9.

22. Kang KM, Lee JM, Yoon JH, Kiefer B, Han JK, Choi BI. Intravoxel Incoherent Motion Diffusion-weighted MR Imaging for Characterization of Focal Pancreatic Lesions. Radiology. 2013.

23. Fujimoto K, Tonan T, Azuma S, et al. Evaluation of the mean and entropy

of apparent diffusion coefficient values in chronic hepatitis C: correlation with pathologic fibrosis stage and inflammatory activity grade. Radiology. 2011;258(3):739-48.

24. Kang Y, Choi SH, Kim YJ, et al. Gliomas: Histogram analysis of apparent diffusion coefficient maps with standard- or high-b-value diffusion-weighted MR imaging--correlation with tumor grade. Radiology. 2011;261(3):882-90.

25. Kim HS, Suh CH, Kim N, Choi CG, Kim SJ. Histogram Analysis of Intravoxel Incoherent Motion for Differentiating Recurrent Tumor from Treatment Effect in Patients with Glioblastoma: Initial Clinical Experience. AJNR American journal of neuroradiology. 2013.

26. Song YS, Choi SH, Park CK, et al. True progression versus pseudoprogression in the treatment of glioblastomas: a comparison study of normalized cerebral blood volume and apparent diffusion coefficient by histogram analysis. Korean journal of radiology : official journal of the Korean Radiological Society. 2013;14(4):662-72.

27. Thoeny HC, De Keyzer F, Vandecaveye V, et al. Effect of vascular targeting agent in rat tumor model: dynamic contrast-enhanced versus diffusion-weighted MR imaging. Radiology. 2005;237(2):492-9.

28. Sun X, Wang H, Chen F, et al. Diffusion-weighted MRI of hepatic tumor in rats: comparison between in vivo and postmortem imaging acquisitions. Journal of magnetic resonance imaging : JMRI. 2009;29(3):621-8.

29. Koh DM, Collins DJ. Diffusion-weighted MRI in the body: applications and challenges in oncology. AJR American journal of roentgenology. 2007;188(6):1622-35.

30. Steens SC, Admiraal-Behloul F, Schaap JA, et al. Reproducibility of brain

ADC histograms. Eur Radiol. 2004;14(3):425-30.

31. Segaloff A. Hormones and breast cancer. Recent progress in hormone research. 1966;22:351-79.

32. Alvarez E, Westmore M, Galvin RJ, et al. Properties of bisphosphonates in the 13762 rat mammary carcinoma model of tumor-induced bone resorption. Clinical cancer research : an official journal of the American Association for Cancer Research. 2003;9(15):5705-13.

33. Sigmund EE, Vivier PH, Sui D, et al. Intravoxel incoherent motion and diffusion-tensor imaging in renal tissue under hydration and furosemide flow challenges. Radiology. 2012;263(3):758-69.

34. Lee J, Koh D, Ong CN. Statistical evaluation of agreement between two methods for measuring a quantitative variable. Computers in biology and medicine. 1989;19(1):61-70.

35. Bland JM, Altman DG. Statistical methods for assessing agreement between two methods of clinical measurement. Lancet. 1986;1(8476):307-10.

36. Padhani AR, Liu G, Koh DM, et al. Diffusion-weighted magnetic resonance imaging as a cancer biomarker: consensus and recommendations. Neoplasia. 2009;11(2):102-25.

37. Joo I, Lee JM, Yoon JH, Jang JJ, Han JK, Choi BI. Nonalcoholic Fatty Liver Disease: Intravoxel Incoherent Motion Diffusion-weighted MR Imaging--An Experimental Study in a Rabbit Model. Radiology. 2013.

38. Jensen LR, Garzon B, Heldahl MG, Bathen TF, Lundgren S, Gribbestad IS. Diffusion-weighted and dynamic contrast-enhanced MRI in evaluation of early treatment effects during neoadjuvant chemotherapy in breast cancer patients. Journal of magnetic resonance imaging : JMRI. 2011;34(5):1099-109.

39. Lambregts DM, Beets GL, Maas M, et al. Tumour ADC measurements in rectal cancer: effect of ROI methods on ADC values and interobserver variability. Eur Radiol. 2011;21(12):2567-74.

40. Koh DM, Blackledge M, Collins DJ, et al. Reproducibility and changes in the apparent diffusion coefficients of solid tumours treated with combretastatin A4 phosphate and bevacizumab in a two-centre phase I clinical trial. Eur Radiol. 2009;19(11):2728-38.

41. Goh V, Ganeshan B, Nathan P, Juttla JK, Vinayan A, Miles KA. Assessment of response to tyrosine kinase inhibitors in metastatic renal cell cancer: CT texture as a predictive biomarker. Radiology. 2011;261(1):165-71.

42. Haralick RM. Statistical and Structural Approaches to Texture. P Ieee. 1979;67(5):786-804.

43. Kobus T, Vos PC, Hambrock T, et al. Prostate cancer aggressiveness: in vivo assessment of MR spectroscopy and diffusion-weighted imaging at 3 T. Radiology. 2012;265(2):457-67.

44. Kyriazi S, Collins DJ, Messiou C, et al. Metastatic ovarian and primary peritoneal cancer: assessing chemotherapy response with diffusion-weighted MR imaging--value of histogram analysis of apparent diffusion coefficients. Radiology. 2011;261(1):182-92.

45. Tozer DJ, Jager HR, Danchaivijitr N, et al. Apparent diffusion coefficient histograms may predict low-grade glioma subtype. NMR in biomedicine. 2007;20(1):49-57.

46. Nowosielski M, Recheis W, Goebel G, et al. ADC histograms predict response to anti-angiogenic therapy in patients with recurrent high-grade glioma. Neuroradiology. 2011;53(4):291-302.

47. Downey K, Riches SF, Morgan VA, et al. Relationship between imaging biomarkers of stage I cervical cancer and poor-prognosis histologic features: quantitative histogram analysis of diffusion-weighted MR images. AJR American journal of roentgenology. 2013;200(2):314-20.

48. Luo H. Generation of Non-normal Data: A Study of Fleishman's Power Method. Uppsala: Department of Statistics, Uppsala University, 2011; p. 29.

49. Pekar J, Moonen CT, van Zijl PC. On the precision of diffusion/perfusion imaging by gradient sensitization. Magn Reson Med. 1992;23(1):122-9.

50. Koh DM, Scurr E, Collins DJ, et al. Colorectal hepatic metastases: quantitative measurements using single-shot echo-planar diffusion-weighted MR imaging. Eur Radiol. 2006;16(9):1898-905.

51. Shinmoto H, Oshio K, Tanimoto A, et al. Biexponential apparent diffusion coefficients in prostate cancer. Magnetic resonance imaging. 2009;27(3):355-9.

52. Lemke A, Laun FB, Klauss M, et al. Differentiation of pancreas carcinoma from healthy pancreatic tissue using multiple b-values: comparison of apparent diffusion coefficient and intravoxel incoherent motion derived parameters. Investigative radiology. 2009;44(12):769-75.

53. Baek HJ, Kim HS, Kim N, Choi YJ, Kim YJ. Percent change of perfusion skewness and kurtosis: a potential imaging biomarker for early treatment response in patients with newly diagnosed glioblastomas. Radiology. 2012;264(3):834-43.

54. Ganeshan B, Miles KA, Young R, Chatwin C. Hepatic entropy and uniformity: additional parameters that can potentially increase the effectiveness of contrast enhancement during abdominal CT. Clin Radiol. 2007;62(8):761-8.

55. Sharma N, Ray AK, Sharma S, Shukla K, Aggarwal L, Pradhan S. Segmentation of medical images using simulated annealing based fuzzy C Means

algorithm. Int J Biomed Eng Technol. 2009;2(3):260-78.

56. Albregtsen F. Statistical texture measures computed from gray level coocurrence matrices. Image Processing Laboratory, Department of Informatics, University of Oslo; 1995 [updated November 5, 2008; cited 2013 September 7]; Available from: http://www.uio.no/studier/emner/matnat/ifi/INF4300/h08/undervisningsmateriale/glcm.pdf.

APPENDIX

1) Skewness and kurtosis

Skewness represents distribution pattern of the degree of pixel value on histograms. Negative and positive Skewness indicated that the pixel values are more spread to the left and right of the mean, respectively (53). Kurtosis represents the position of peak height that indicates pixel value of the maximum frequency on histograms. Normal distribution has a kurtosis 0, leptokurtic, which is indicated by a sharper peak, has a kurtosis >0 and platykurtic, which is indicated by a flatter peak, has a kurtosis <0 (53). Parameters are defined mathematically below, where N the number of data points in region-of-interest, $\overline{X}$ the mean and s the standard deviation.

$$\text{Skewness} = \frac{1}{(N-1)s^3}\sum_{i=1}^{N}\left(X_i - \overline{X}\right)^3$$

$$\text{Kurtosis} = \frac{1}{(N-1)s^4}\sum_{i=1}^{N}\left(X_i - \overline{X}\right)^4$$

2) Entropy and homogeneity

Heterogeneity within the tumor was assessed with entropy and homogeneity. Entropy is a term that has been widely used in information theory as a parameter that reflects the unpredictability or information content of an image (54). Homogeneity is the measure that increases with less contrast in the window, and was calculated using the two-dimensional image histogram in this study (55). High entropy and low homogeneity values indicate increased heterogeneity of the tumor.

Parameters are defined mathematically below, where G the number of gray levels in region-of-interest and P(I) the probability of the occurrence of the gray level I on histogram.

$$\text{Entropy} = -\sum_{i=1}^{G}[P(I)]\log_2[P(I)]$$

$$\text{Homogeneity} = \sum_{i=1}^{G-1}\sum_{j=1}^{G-1}\frac{1}{1+(I-J)}P(I,J)$$

3) Texture parameters from gray-level co-occurrence matrix (GLCM)

A GLCM is a matrix where the element P(i, j) is relative frequency with which a combination of two pixels with intensity i and j occur in an image, separated by a given distance. A number of texture features may be extracted from the GLCM and two texture features calculated from the GLCM were used in this study. GLCM inverse difference moment (IDM) is influenced by the homogeneity of the image and GLCM contrast reflects the local intensity variation (56).

$$\text{GLCM IDM} = \sum_{i=0}^{G-1}\sum_{j=0}^{G-1}\frac{1}{1+(i-j)^2}P(i,j)$$

$$\text{GLCM contrast} = \sum_{\mathrm{n}=0}^{\mathrm{G}-1}\mathrm{n}^2\left\{\sum_{\mathrm{i}=1}^{\mathrm{G}}\sum_{\mathrm{j}=1}^{\mathrm{G}}\mathrm{P(i,j)}\right\}, \qquad |\mathrm{i}-\mathrm{j}| = \mathrm{n}$$

국 문 초 록

목적: 쥐 FN13762 유방암의 복셀 내 화소 결집 운동 확산 강조 영상에서 얻은 히스토그램 및 텍스처 파라미터들의 재현성을 평가한다.

방법: 이 연구는 동물실험윤리위원회의 허가를 받았다. Fisher 344 쥐 11 마리의 우측 뒷다리 상단부에 FN13762 설치류 유방암 세포(5×10^6)를 심었다. 종양 이식 9 일 후, 9 개의 b 값을 사용한 복셀 내 화소 결집 운동 확산 강조 영상을 3T 자기공명 스캐너로 두 차례 촬영하였다. 한 명의 영상의학과 전공의가 수동으로 종양 전체를 포함하도록 흥미영역을 그렸고 자체 개발한 소프트웨어를 이용해 현성확산계수, 진성확산계수, 가성확산계수, 관류 분율 지도로부터 히스토그램 및 텍스처 파라미터들을 계산하였다. 관찰자내 및 촬영간 측정 재현성을 대응비교 t 검증, 급내상관계수 및 Bland−Altman 방법으로 평가하였다.

결과: 흥미영역의 평균 부피는 우수한 관찰자내 및 촬영간 일치도를 보였으며 계통적 비뚤림은 없었다. 현성확산계수 지도로부터 계산된 평균, 엔트로피, 5 백분위수, 10 백분위수, 25 백분위수 및 90 백분위수와 진성확산계수 지도로부터 얻은 평균, 엔트로피, 그레이 레벨 동시발생 행렬 콘트라스트, 5 백분위수, 10 백분위수, 25 백분위수 및 50 백분위수가 우수한 관찰자내 및 촬영간 일치도를 보였으며 (급내상관계수의 95% 신뢰하한 ≥0.75) 계통적 비뚤림도 보이지 않았다. 가성확산계수 및 관류 분율 지도로부터 얻은 모든 파라미터는 상대적으로 우수하지 못한 관찰자내 및 촬영간 일치도를 보였다 (급내상관계수의 95% 신뢰하한 <0.75).

결론: 히스토그램 및 텍스처 분석은 현성확산계수 및 진성확산계수 지도에서 시행하는 것이 가성확산계수 및 관류 분율 지도에서 시행하는 것에 비해 측정 재현성 면에서 유리하다.

……

주요어: 재현성, 히스토그램, 텍스처, 복셀 내 화소 결집 운동, 확산 강조 영상, FN13762 쥐 유방암
학 번: 2012-21696